ACS Catalysis

Research Article

pubs.acs.org/acscatalysis

Robust Mesoporous Manganese Oxide Catalysts for Water Oxidation

Chung-Hao Kuo,[†] Islam M. Mosa,[†,‡] Altug S. Poyraz,[†] Sourav Biswas,[†] Abdelhamid M. El-Sawy,[†,‡] Wenqiao Song,[†] Zhu Luo,[†] Sheng-Yu Chen,[†] James F. Rusling,[†] Jie He,[†] and Steven L. Suib*[,†,§]

[†]Department of Chemistry, University of Connecticut, U-3060, 55 North Eagleville Road, Storrs, Connecticut 06269, United States

[‡]Department of Chemistry, Faculty of Science, Tanta University, Tanta 31527, Egypt

[§]Institute of Materials Science, University of Connecticut, U-3060, 55 North Eagleville Road, Storrs, Connecticut 06269, United States

Supporting Information

ABSTRACT: Inspired by the natural oxygen evolution reaction of Photosystem II, the earth-abundant and inexpensive manganese oxides (MnO_x) have been recognized for their great potential as highly efficient and robust materials for water oxidation reaction (WORs). To date, most of the heterogeneous, synthesized MnO_x catalysts still exhibit lower activities for WORs, in comparison to RuO_2 and IrO_2. Herein, we report a single-step and scalable synthesis method for mesoporous MnO_x materials that is developed through a soft-templated method. This method allowed precise control of Mn^{3+}-rich Mn_2O_3 structure as well as pore sizes and crystallinity of these mesoporous MnO_x. These catalysts were investigated for both photochemical and electrochemical water oxidation, and they presented a superior activity for water oxidation. The highest turnover frequency of 1.05×10^{-3} s^{-1} was obtained, which is comparable with those for precious metal oxide based catalysts (RuO_2 and IrO_2). Our results illustrate a guideline to the design and synthesis of inexpensive and highly active heterogeneous catalysts for water oxidation.

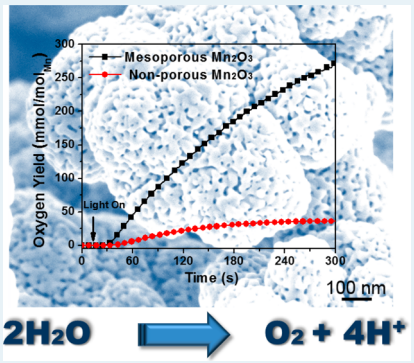

KEYWORDS: *water splitting, catalysis, oxygen evolution reaction, mesoporous material, manganese oxide*

1. INTRODUCTION

The design of highly active catalysts for solar-driven water oxidation reactions (WORs) is critical to develop integrated artificial photosynthetic systems. Inspired by the Photosystem II system catalyzed by Mn tetramer clusters of $CaMn_4O_5$,[1−3] earth-abundant and inexpensive manganese oxides (MnO_x) have been recognized for their great potential as highly efficient and robust catalysts of WORs.[4] However, the documented catalytic activity of MnO_x for WORs is still rather low: at least 1 order of magnitude lower than that of IrO_2 and RuO_2. In order to improve the catalytic activity of MnO_x, much effort has been devoted to the study of structural properties: e.g., the valence of Mn centers and the surface properties of catalysts.[5−11] Mn^{3+} species having longer Mn−O−Mn bonds were found to be much more active for WORs than Mn^{2+}/Mn^{4+} species. Mn^{3+}-rich structures with labile Mn−O bonds allow for the formation of surface $Mn-OH_2$ species and the cleavage of $Mn-O_2$ bonds, which facilitates WORs and increases the overall turnover frequency (TOF) of the catalytic centers.[12−16] The controllable synthesis of MnO_x with enriched Mn^{3+} species is therefore highly desired. In addition, the control of surface properties of MnO_x catalysts, e.g. surface area and surface oxygen mobility,[5,17] is known to be very critical for WORs as well. For instance, mesoporous catalysts exhibited better catalytic performance for WORs in comparison to bulk catalysts.[18−20] Jiao et al. reported that nanometer-sized MnO_x catalysts supported on mesoporous silica were highly active for WORs.[19] The high surface area of the silica support played a critical role in the performance of these catalysts. However, the preparation of mesoporous MnO_x catalysts via the hard template approach involves a complicated and time-consuming process that limits the practical applications of those materials. Moreover, the precise control over the crystallinity and valence of MnO_x-based transition-metal oxides is still challenging due to the different possible coordination numbers and oxidation states of Mn centers.

Herein, we report a facile and general synthesis of high-quality mesoporous MnO_x with the crystal structure of Mn_2O_3 using a one-step inverse micelle templating approach.[21] Our synthesis procedure involves a simple sol−gel process using manganese nitrate as a precursor and nonionic surfactant P123 as a soft template. By varying the calcination temperature, manipulation of the crystal structures and size of the Mn_2O_3 phase of the materials from the amorphous to the bixbyite Mn_2O_3 structure is possible. In comparison to previous species prepared by a nanocasting (using a hard template) approach, our synthetic approach has the advantages of (i) being a single-step wet-chemical synthesis without any post-treatment, (ii) producing large quantities of mesoporous Mn_2O_3 materials on gram scales, (iii) tuning the pore size, surface area, and

Received: November 4, 2014
Revised: January 13, 2015
Published: February 6, 2015

DOI: 10.1021/cs501739e
ACS Catal. 2015, 5, 1693−1699

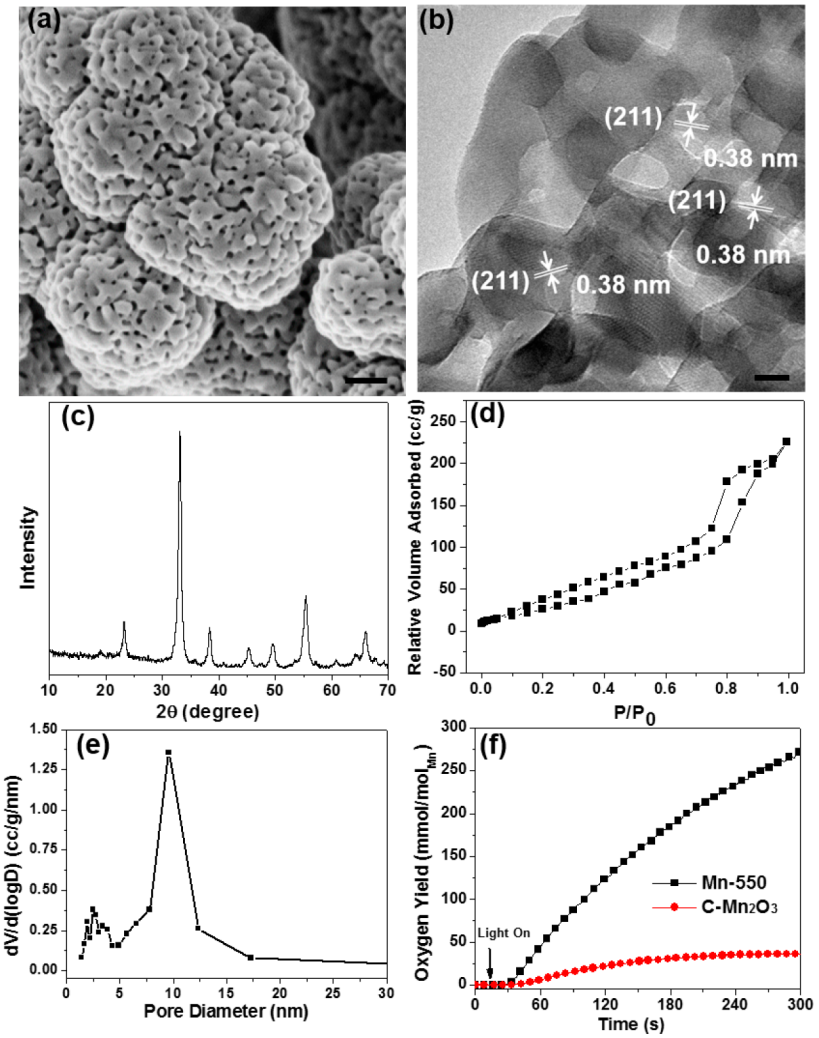

Figure 1. (a) SEM and (b) high-resolution TEM images of mesoporous Mn-550 catalyst. The measured lattice distance of 0.38 nm in (b) is correlated with the (211) plane of bixbyite α-Mn_2O_3 structures. Scale bars are 50 nm in (a) and 10 nm in (b). (c) Powder XRD pattern of Mn-550 catalyst. (d) Nitrogen adsorption isotherm and (e) BJH desorption pore distribution diagram of the Mn-550 catalyst. (f) Dissolved oxygen concentration of photochemical water oxidation for Mn-550 and C-Mn_2O_3 (commercial Mn_2O_3) catalysts. Conditions: 1.5 mM of $Ru(bpy)_3^{2+}$, 13 mM of $Na_2S_2O_8$, 68 mM of Na_2SO_4, and 3 mg of catalysts in 15 mL of Na_2SiF_6–$NaHCO_3$ buffer solution (pH ~5.8). The WOR results were confirmed by at least three individual measurements.

crystallinity of Mn_2O_3 materials, and (iv) most importantly, precisely controlling the valence transition of MnO_x to enrich the amount of Mn^{3+}. The mesoporous Mn_2O_3 materials exhibit superior activities for photocatalytic WORs. A TOF of 1.05×10^{-3} s^{-1} for WORs, to the best of our knowledge, is the highest TOF using synthetic MnO_x reported so far.[2,4,5,7,8]

2. EXPERIMENTAL SECTION

2.1. Materials. Manganese(II) nitrate tetrahydrate ($Mn(NO_3)_2{\cdot}4H_2O$, ≥97%), 1-butanol (anhydrous, 99.8%), nitric acid (HNO_3, 68–70%), Mn_2O_3 (99%, ~325 mesh), poly(ethylene glycol)-*block*-poly(propylene glycol)-*block*-poly(ethylene glycol) (PEO_{20}-*b*-PPO_{70}-*b*-PEO_{20}, Pluronic P123), Na_2SiF_6, $Na_2S_2O_8$, Na_2SO_4, and $NaHCO_3$ were purchased from Sigma-Aldrich and used without further purification unless otherwise noted. K-Cryptomelane α-MnO_2, K-Birnessite δ-MnO_2, and amorphous manganese oxide (AMO) were synthesized by following literature procedures.[5] The [$Ru(bpy)_3^{2+}$] photosensitizer tris(2,2′-bipyridyl)ruthenium(II) chloride hexahydrate (98%) and commercial RuO_2 were obtained from Strem Chemical Inc. and used as received. The ultrapure water was obtained using a High-Q, Inc. system (Model 103S) with a resistivity of >10.0 MΩ.

2.2. Synthesis of Mesoporous Mn_2O_3. Manganese(II) nitrate tetrahydrate (1.2 g, 4.78 mmol) was first dissolved in *n*-butanol (10 g, 0.13 mol), HNO_3 (~3.5 g in 68% solution, 0.38 mol), and P123 surfactant (1.2 g) in a 150 mL beaker at room temperature with strong stirring. The solution was then placed in a preheated oven at 120 °C for 3 h. The obtained deep brown powder was washed several times with ethanol to remove the excess surfactant by centrifugation. The final powder product was dried at 40 °C under vacuum overnight. The dry powder was then subjected to heating cycles to achieve the desired crystal structures and mesopore sizes. The sample was first heated at 150 °C for 12 h. The collected material was denoted as Mn-150. The further heating processes were followed by 250 °C for 6 h, 350 °C for 4 h, 450 °C for 2 h, and 550 °C for 1 h, and the obtained samples were denoted as Mn-250, Mn-350, Mn-450, and Mn-550, respectively. All heat treatments were done in an air atmosphere. *Caution!* The

DOI: 10.1021/cs501739e
ACS Catal. 2015, 5, 1693–1699

annealing treatment of all samples was performed in ovens with proper ventilation due to release of toxic NO_x gas from the gel.

2.3. Water Oxidation Reaction of Mesoporous Mn_2O_3. Photochemical water oxidation tests were conducted in a 20 mL quartz reaction vessel containing 3 mg of the catalyst, 1.5 mM $Ru(bpy)_3^{2+}$, 13 mM $Na_2S_2O_8$, and 68 mM Na_2SO_4 in 15 mL of buffered aqueous solutions (0.022−0.028 M Na_2SiF_6−$NaHCO_3$ solution with pH ∼5.8). Reactants in the quartz vessel were sonicated for 1 min and purged with argon for 5 min to remove all dissolved oxygen from the aqueous solution. The quartz vessel was then irradiated with a continuous output xenon lamp (250 W). A cutoff filter (λ >400 ± 10 nm, SCHOTT North America, Inc.) was placed between the quartz vessel and the light source to remove UV light. The amount of dissolved oxygen was measured using an automatic temperature-compensated needle-type oxygen microsensor based on a 140 μm optical fiber (Microx TX3-trace, Presens).

2.4. Electrochemical Oxygen Evolution Study. Linear sweep voltammetry (LSV), electrochemical impedance (EIS), and chronopotentiometry experiments were obtained with a CHI 660A electrochemical workstation. For electrochemical oxygen evolution studies, pyrolytic graphite carbon working electrodes were used (surface area ∼0.14 cm^2) equipped with a rotating-disk working electrode (RDE) configuration. A platinum wire was used as a counter electrode and a saturated calomel electrode (SCE) as the reference electrode. The potentials reported in this work are referenced to the reversible hydrogen electrode (RHE) and denoted as RHE potential. The preparation of the working electrode is as follows: 4 mg of catalysts and 0.4 mg of carbon (VulcanXC-72) were dispersed in 2 mL of water/EtOH by sonication. Then, 19 μL of Nafion solution was added and sonicated for another 20 min. A 15 μL portion of the solution mixture was dropped on the working electrode surface and dried overnight before use. CV curves were *i*R-compensated and measurements performed from 1.21 to 1.81 V (vs RHE) with a sweep rate of 5 mV s^{-1} in oxygen-saturated 0.1 M KOH solution. The working electrode was rotated at 1600 rpm. The electrochemical impedance spectra were applying an ac voltage with 5 mV amplitude in a frequency range from 0.01 to 100 kHz for five cycles. To check the fitting results, selected experimental data were also fitted using the ZSimDemo software package (version 3.2). In this procedure, RC initial estimates were obtained using a circle fitting function. Similar fitting parameters were obtained using both software packages. For chronopotentiometric tests, the current density was fixed at 5 mA/cm^2 for the anodic reaction.

The calculation of mass activity and TOF of electrochemical studies in this work is based on literature published by Guo et al.[22] Mass activity (A g^{-1}) values were obtained from depositing the catalytic materials on the working electrode (∼0.03 mg) with measured current density (j, A cm^{-2}) at η = 0.35 V. Turnover frequency (TOF) values were obtained using the following equation, assuming all materials on the working electrode are involved in the reaction: TOF = $jS/4Fn$, where j (A cm^{-2}) is the measured current density at η = 0.35 V, S (cm^2) represents the surface area of the working electrode, F (C mol^{-1}) is the Faraday constant, 4 is the number of the electrons involved in the reaction, and n (mol) is the moles of the metal atom on the working electrode.

3. RESULTS AND DISCUSSION

The synthetic procedures of mesoporous Mn_2O_3 catalysts are given in the Experimental Section.[21,23] Briefly, manganese(II) nitrate, P123, and nitric acid were first dissolved in *n*-butanol. After it was stirred for 30 min to generate a homogeneous clear solution, the reaction mixture was placed in an oven running at 120 °C for 3 h. The collected solids were further washed with excess ethanol to remove the surfactant (solvent extraction). In order to maintain the mesoporosity of the materials, a stepwise annealing process was utilized for the structural transformation of the amorphous structure to crystalline mesoporous Mn_2O_3. The materials were subjected to an annealing cycle between 150 and 550 °C and denoted as Mn-150−Mn-550 hereafter. The mesoporous Mn-550 catalyst was studied by scanning electron microscopy (SEM) and transmission electron microscopy (TEM), as shown in Figure 1a,b. The SEM image clearly showed the porous structure of the material. The crystal domain size of Mn_2O_3 as well as its pore size are in the range 10−20 nm. High-resolution TEM analysis showed the crystalline bixbyite structure of Mn_2O_3. The measured d spacing of 0.38 nm is attributed to the (211) plane of Mn_2O_3. The powder X-ray diffraction (PXRD) pattern clearly shows the main diffraction peaks of the (211), (222), (400), (332), (431), (440), and (622) planes, confirming the bixbyite Mn_2O_3 structures.[24] The size of aggregated Mn_2O_3 nanoparticles estimated from the Scherrer equation is approximately 17.3 nm, which is consistent with our TEM observations. The mesoporosity with uniform pore size distribution of Mn-550 was confirmed by a type IV nitrogen adsorption isotherm followed by a type I hysteresis loop. The Brunauer−Emmett−Teller (BET) surface area of Mn-550 was estimated to be 120 m^2 g^{-1} with a pore size of 9.6 nm and a pore volume of 0.42 cm^3 g^{-1}.

Photocatalytic water oxidation was studied using a $Ru(bpy)_3^{2+}$−$Na_2S_2O_8$ system ($E(Ru^{3+}/Ru^{2+})$ = 1.24 V) and mesoporous Mn-550 as a catalyst.[5] The overall photochemical reaction of the WOR is $2Ru(bpy)_3^{2+} + S_2O_8^{2-} + h\nu \rightarrow 2Ru(bpy)_3^{3+} + SO_4^{2-}$, where $S_2O_8^{2-}$ is the sacrificial electron acceptor. The generated Ru^{3+} species can be reduced back to Ru^{2+} by removing one electron from the Mn catalyst while water molecules are oxidized to form O_2 by losing electrons to the catalysts. The evolved oxygen concentration was monitored using a needlelike oxygen microsensor (temperature compensated optic oxygen meter). The Mn-550 material showed a superior activity for oxygen evolution under these conditions (Figure 1f). The dissolved oxygen content quickly increased to 270 mmol/mol of Mn after 6 min of irradiation. The TOF number of Mn-550 reached 1.05×10^{-3} s^{-1}, which is nearly 1 order of magnitude higher than that of a commercial Mn_2O_3 (C-Mn_2O_3) material which has a TOF of 1.85×10^{-4} s^{-1}. This TOF value is the highest among the synthetic manganese oxides (see Table S1 in the Supporting Information). Mn_2O_3 materials are known to be the most active phase for water oxidation among all manganese oxide phases.[2,12] As a comparison, commercial RuO_2 and Mn_2O_3 were also tested under the same reaction conditions. RuO_2 has a TOF of 3.87×10^{-3} s^{-1}, which is much higher than that of C-Mn_2O_3, whereas the Mn-550 activity was comparable to that of RuO_2 materials. Such a dramatic enhancement in WOR catalytic activity is presumably because of the high surface area and the uniform mesoporous size distribution of the Mn-550 material.

To understand the correlation between the nanostructures and catalytic performance of mesoporous Mn_2O_3 catalysts, we further investigated the effect of calcination temperatures on the catalytic performances of mesoporous Mn_2O_3 catalysts. The mesoporous MnO_x catalysts calcined at lower temperatures

DOI: 10.1021/cs501739e
ACS Catal. 2015, 5, 1693−1699

(mesoporous Mn-150, -250, and -350) exhibited poor crystallinity, as they were shown to be nearly amorphous by XRD (see Figure 2a). Upon calcination at temperatures of 450 °C and higher, the bixbyite Mn_2O_3 structure was identified. Table 1 summarizes the physicochemical properties of mesoporous materials obtained at different calcination temperatures. The surface areas of all mesoporous materials are in the range 129−226 m^2/g, much higher than that of C-Mn_2O_3 (11 m^2/g). The pore size and pore volume increased solely with calcination temperature due to the increase in nanoparticle size.[21] The crystal domain size of mesoporous Mn_2O_3 was also enhanced with an increase in calcination temperature, as was observed from low-angle XRD diffraction peaks (see Figure S9 in the Supporting Information). For example, the crystal domain size of Mn-150 is ∼2.6 nm, while Mn-450 has a crystal domain size of ∼11.5 nm. The structural evolution of mesoporous Mn_2O_3 materials obtained at different calcination temperatures was investigated using Raman spectroscopy (see Figure 2b). For Mn-150 and Mn-250 samples, one strong band at 646 cm^{-1} can be assigned to the Mn−O breathing mode of the divalent Mn ions in tetrahedral coordination and the other small peak at the range of 200−400 cm^{-1} may correspond to asymmetric stretching of bridging oxygen species (Mn−O−Mn). These spectra are very similar to those of reported amorphous manganese oxide (AMO),[5] suggesting that Mn-150 and Mn-250 possibly consist of layered hydroxides. At higher calcination temperatures, new peaks at 311 and 570−770 cm^{-1} arise, which can be attributed to the out-of-plane bending modes and symmetric stretching of bridging oxygen species (Mn−O−Mn), respectively.[25] These vibrational bands are identical with the Raman spectrum of C-Mn_2O_3, further confirming the structural transition of MnO_x materials from amorphous layered structures to bixbyite Mn_2O_3. The transition temperature of MnO_x materials in Raman studies is obviously lower than that in XRD results. This is possibly because of the low crystallinity of MnO_x calcined at 350 °C that cannot be observed using XRD.

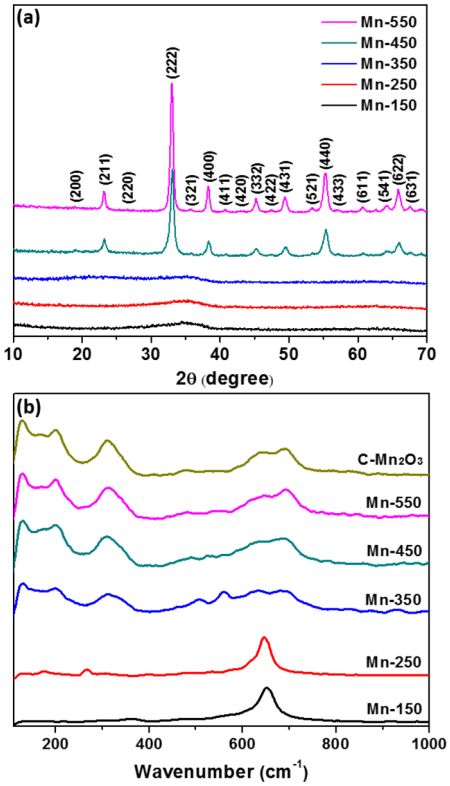

Figure 2. (a) Powder XRD patterns and (b) Raman spectra for synthesized mesoporous MnO_x catalysts with different calcination temperatures. The observed main diffraction peaks of Mn-450 and -550 in (a) are ascribed to bixbyite Mn_2O_3 (211), (222), (400), (332), (431), (440), and (622) planes.

The WOR activities of all samples obtained at different calcination temperatures were studied under identical conditions (Figure 3). The dissolved oxygen content quickly increased with an increase in calcination temperature, indicating the enhanced catalytic activity for WORs. The turnover number of the Mn-150 sample is 1.51×10^{-4} s^{-1}, close to that of the nonporous C-Mn_2O_3 sample (see Table 2). The crystalline mesoporous Mn_2O_3 catalysts calcined at 450 °C (Mn-450) and 550 °C (Mn-550) obviously exhibited higher activity than the ones calcined at lower temperatures. The TOF number

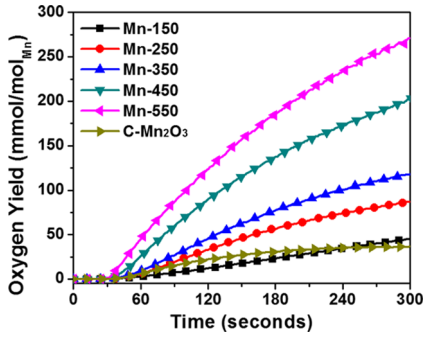

Figure 3. Dissolved oxygen concentration of photochemical water oxidation for mesoporous manganese oxide materials calcined at different temperatures. Conditions: 1.5 mM of $Ru(bpy)_3^{2+}$, 13 mM of $Na_2S_2O_8$, 68 mM of Na_2SO_4, and 3 mg of catalyst in 15 mL of Na_2SiF_6−$NaHCO_3$ buffer solution (pH ∼5.8). The WOR results were confirmed by at least three individual measurements.

Table 1. Structural Parameters of Mesoporous Manganese Oxide Materials

material	S_{BET} (m^2 g^{-1})[a]	P (nm)[b]	V (cm^3 g^{-1})[c]	L (nm)[d]	D (nm)[e]	cryst structure (XRD)
Mn-150	129	2.7	0.21	2.6	N/A	amorphous
Mn-250	182	3.4	0.24	7.8	N/A	amorphous
Mn-350	226	3.4	0.24	8.1	N/A	amorphous
Mn-450	150	4.3	0.26	11.5	11.4	Mn_2O_3 (bixbyite)
Mn-550	120	9.6	0.42	N/A	17.3	Mn_2O_3 (bixbyite)
C-Mn_2O_3	11	N/A	N/A	N/A	35.4	Mn_2O_3 (bixbyite)

[a]Surface area obtained from Brunauer−Emmett−Teller (BET) measurements (S_{BET}). [b]BJH desorption pore size distribution (P). [c]BJH desorption pore volume (V). [d]Low-angle XRD peak position (L). [e]Scherrer's crystallite size (D).

DOI: 10.1021/cs501739e
ACS Catal. 2015, 5, 1693−1699

Table 2. Summarized WOR and OER Activities of Mesoporous Manganese Oxide Catalysts

catalyst	η at J = 10 mA cm^{-2} (mV)	mass activity at η = 0.35 V (A g^{-1})[a]	resistance R_{ct} (Ω)	TOF at η = 0.35 V (s^{-1})	TOF of WOR
MnO-150	N/A[a]	2.75	567	1.57×10^{-4}	1.51×10^{-4}
MnO-250	N/A[a]	21.02	394	1.20×10^{-3}	3.15×10^{-4}
MnO-350	575	25.83	284	1.48×10^{-3}	4.31×10^{-4}
MnO-450	507	35.23	165	2.01×10^{-3}	7.70×10^{-4}
MnO-550	N/A[a]	9.60	539	5.49×10^{-4}	1.05×10^{-3}
C-Mn_2O_3	N/A[a]	2.48	1530	1.42×10^{-4}	1.85×10^{-4}
RuO_2	415	183.62	168	1.15×10^{-2}	3.87×10^{-3}

[a]Failed to reach J = 10 mA/cm^{-2} under our experimental conditions.

increased from 4.31×10^{-4} to 7.70×10^{-4} s^{-1} when the calcination temperature was increased from 350 to 450 °C. The formed Mn^{3+}-rich crystalline Mn_2O_3 structures of Mn-450 were believed to be crucial in the improvement of catalytic activity. When the calcination temperature was increased to 550 °C, the TOF of Mn-550 increased to 1.05×10^{-3} s^{-1}, even though the surface area started to decrease.

Electrochemical oxygen evolution reactions (OERs) of mesoporous Mn_2O_3 materials were further explored to confirm the WOR results. Using the rotating-disk electrode (RDE) system in a three-electrode chemical cell, linear sweep voltammetry (LSV) was done in an oxygen-saturated 0.1 M KOH solution with a scan rate of 5 mV s^{-1} and a rotation speed of 1600 rpm. The catalytic materials were mounted on the surface of pyrolytic graphite carbon working electrodes before the measurements. The OER results are summarized in Figure 4a and Table 1. The OER activities of all materials showed trends similar to those of the photochemical systems, except for Mn-550. Mn-450 exhibited the highest activity for OERs. The overpotential (η) of Mn-450 at a current density of 10 mA cm^{-2} is 507 mV. The calculated TOF of Mn-450 at η = 350 mV is 2.01×10^{-3}, which is higher than TOF value (7.70×10^{-4}) from the photochemical system. Again, in comparison to the nonporous C-Mn_2O_3 with a TOF of 1.42×10^{-4}, Mn-450 is at least 1 order of magnitude more active. From Figure S15 in the Supporting Information, the derived Tafel plot showed that Mn-450 has the highest exchange current value. Commercial RuO_2 was also tested for OERs under similar conditions. RuO_2 shows a lower overpotential (η = 415 mV) in comparison to that of Mn-450. However, the current density of Mn-450 approached that of RuO_2 after η > 550 mV, suggesting that the electron transfer rate of Mn catalysts may increase more quickly with an increase of applied potential. Furthermore, the durability of the catalysts was examined by chronopotentiometry at a current density of 5 mA/cm^2 (Figure S17 in the Supporting Information). The results demonstrate that Mn-450 has a good electrochemical stability along with activity, as the overpotential remained nearly constant for more than 10 h. Moreover, the original Mn_2O_3 crystal structure and mesoporosity did not show obvious changes after the reaction (Figure S18 in the Supporting Information). In case of pure RuO_2 catalyst, instability is a disadvantage with long charge–discharge cycling tests, even though the activity is higher.[26] Therefore, when the above performance factors are combined, mesoporous manganese oxide (Mn-450) is both more durable and more feasible than RuO_2.

The electrochemical impedance spectroscopy (EIS) technique was used to elucidate the kinetics and mechanism of oxygen evolution.[27−29] The low-frequency area of the Nyquist plot (Z_{real} vs $-Z_{im}$) was presented, corresponding to the charge transfer resistance (R_{ct}) of the catalytic materials. The fitted

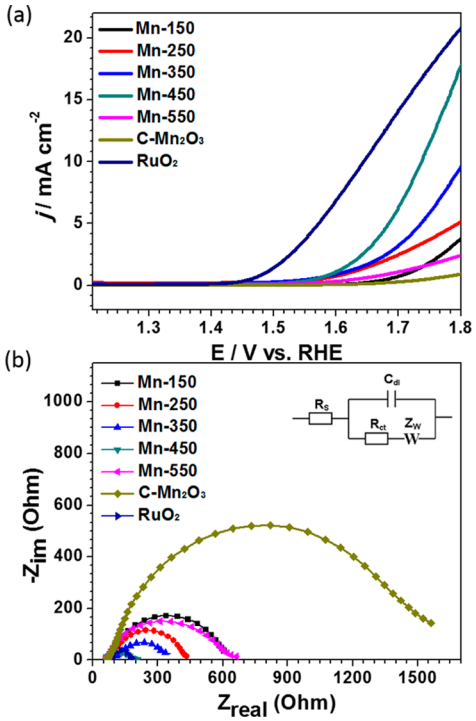

Figure 4. (a) Linear sweep voltammetry curves for mesoporous MnO_x materials for electrochemical oxidation of water with comparison to RuO_2. (b) Nyquist plot at a frequency region of 0.1−100000 Hz obtained from electrochemical impedance measurements at an applied potential of 1.71 V (vs RHE). All measurements were carried out in O_2-purged 0.1 M KOH solution at a scan rate of 5 mV s^{-1} with a RDE at a rotation rate of 1600 rpm. The inset graph represents a fitted equivalent circuit model used to obtain charge transfer resistance of the OER catalysts. Definitions: R_s, active electrolyte resistance; C_{dl}, double-layer capacitance; R_{ct}, active charge transfer resistance; Z_w, specific electrochemical element of diffusion W.

equivalent circuit and model are presented in Figure 4b. First, the R_{ct} value of commercial Mn_2O_3 is 1530 Ω, while all mesoporous Mn_2O_3 materials have much lower R_{ct} values in the range of 165−567 Ω on measurement under the same experimental conditions. R_{ct} values increase in the order Mn-450 > Mn-350 > Mn-250 > Mn-550 > Mn-150. The R_{ct} value is inversely proportional to the electron transfer rate. Therefore, a lower R_{ct} value means the material has a faster electron transfer rate and can be correlated with higher activity in OERs. Overall, the measured R_{ct} values are consistent with the OER activities. Second, Mn-450 has an R_{ct} value similar to that of RuO_2 (165 and 168 Ω, respectively). Such enhanced kinetics may be ascribed to the formation of a highly crystalline Mn_2O_3 phase at 450 °C that subsequently increases the electronic conductivity of the electrode.

DOI: 10.1021/cs501739e
ACS Catal. 2015, 5, 1693−1699

As structural or surface Mn^{3+} species can act as precursors for oxygen production in WORs, a higher Mn^{3+} content might be responsible for the higher WOR activity. To determine the Mn^{3+} content of the catalysts, all mesoporous MnO_x species were first studied by X-ray photoelectron spectroscopy (XPS). XPS spectra of the mesoporous MnO_x materials in the Mn 2p region are shown in Figure S10 and Table S2 in the Supporting Information. The Mn $2p_{3/2}$ binding energy slightly decreased from 642.3 eV for Mn-150 to 642.1 eV for Mn-550, indicating an increase of the Mn valence at higher calcination temperatures. The deconvolution of the Mn $2p_{3/2}$ peak revealed that the ratio of $Mn^{3+}/Mn^{2+/4+}$ increased with calcination temperature (Table S2). This further confirmed the phase transition from amorphous hydroxides to an Mn^{3+}-rich Mn_2O_3 phase with the heat treatment.[30] More detailed valence studies of Mn centers were carried out, using Mn K-edge X-ray absorption near-edge structure (XANES) analysis (Figure 5). To identify

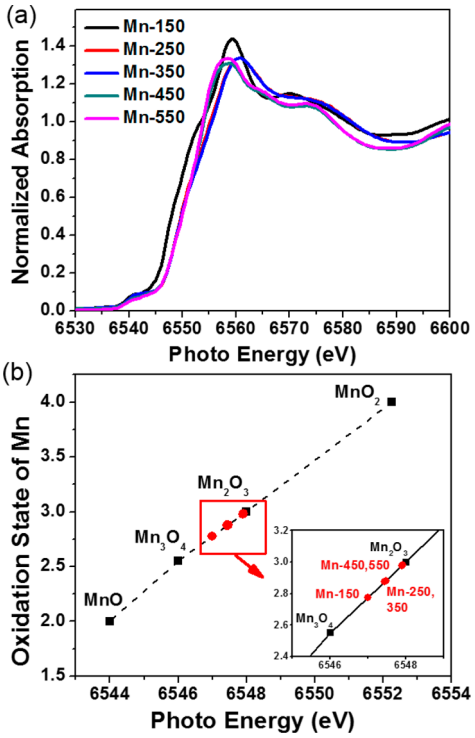

Figure 5. (a) X-ray absorption near-edge spectra (XANES) of Mn K-edge spectra of mesoporous Mn_2O_3 materials depicted with a normalized *Y* axis. (b) Average oxidation state of Mn for mesoporous Mn_2O_3 materials derived from an Mn K-edge absorption threshold.

Mn oxidation states, the Mn K-edge absorption threshold was determined from the first derivative of the near-edge region and least-squares linear combination fitting was used, accompanied by reference samples.[31,32] Accordingly, the average oxidation state of mesoporous MnO_x materials was found to be gradually increasing from 2.77 to 2.97 (~0.4 eV edge shift) when the calcination temperature was increased from 150 to 550 °C. The final valence of Mn was very close to that of the commercial Mn_2O_3 standard sample. The results clearly showed the oxidization of MnO_x materials during calcination and structure transformation from amorphous hydroxides to bixbyite Mn_2O_3 structures.

Another structural parameter that might be also important for the enhanced catalytic activity is the high, accessible surface area of these crystalline mesoporous materials. Unlike conventional mesoporous materials, the mesopores in these materials are formed by connected intraparticle voids formed between the close-packed nanocrystals of manganese oxide. The mesopores formed by intraparticle voids show higher thermal stability for applied heat treatments (up to 550 °C), resulting in highly crystalline wall structures. Therefore, one can use the combined advantages of the Mn_2O_3 phase and high surface areas for WOR catalysis. The more exposed (accessible) catalyst surface minimizes the mass-transfer limitation and increases the catalytic activity.[33] In order to better evaluate the roles of surface area and crystallinity, we calculated the normalized (with respect to surface area) TOFs of WORs. The most crystalline C-Mn_2O_3 sample showed the highest surface area normalized activity, indicating the crucial role of crystallinity. However, the less crystalline Mn-450 sample has higher total activity due to the significantly higher surface area (150 $m^2\ g^{-1}$ vs 11 $m^2\ g^{-1}$) despite having lower normalized WOR activity (see Table 1). The increase of crystallinity can decrease the trapping of electrons or charge recombination during water oxidation and enhance the electron transfer rate. Similar results have already been reported in TiO_2-related materials.[34,35] However, mesoporous manganese oxides showed better catalytic activity than their commercial analogue (C-Mn_2O_3) because of both their crystalline nature and high surface area.

4. CONCLUSION

In summary, mesoporous MnO_x with tunable mesoporosity and crystallinity along with high surface areas were synthesized via a single-step soft-templated (inverse surfactant surfactant micelles) wet-chemistry approach. The pore sizes as well as the crystallinity of mesoporous MnO_x catalysts can be well-controlled by a simple calcination process without the collapse of mesoporosity. The mesopore sizes can be controlled precisely in the range of ~2.5−10 nm while preserving a high surface area (up to 226 m^2/g). The MnO_x materials showed superior activities for WORs and OERs compared to nonporous commercial Mn_2O_3 catalysts. The highest TOF value ($1.05 \times 10^{-3}\ s^{-1}$) was achieved by the sample calcined at 550 °C (Mn-550). These TOF numbers are comparable to the most active RuO_2 ($3.87 \times 10^{-3}\ s^{-1}$). The enhanced catalytic activity is correlated with the increase of Mn^{3+} concentration (in a highly crystalline Mn_2O_3 phase) with increasing calcination temperature, as confirmed by XPS and XANES studies. The high surface area of the mesoporous manganese oxide samples was found to be another crucial parameter dictating the catalytic activity. Our study illustrates a general guideline to the design and synthesis of inexpensive and highly active heterogeneous catalysts for water oxidation.

■ ASSOCIATED CONTENT

Supporting Information

The following file is available free of charge on the ACS Publications website at DOI: 10.1021/cs501739e.

Detailed material characterization, including N_2 sorption (pore size distribution), low-angle XRD, TEM, SEM, XPS, and XANES, and a summary of the photochemical activities on manganese oxide materials published in the literature and other electrochemical studies (PDF)

DOI: 10.1021/cs501739e
ACS Catal. 2015, 5, 1693−1699

AUTHOR INFORMATION

Corresponding Author

*S.L.S.: e-mail, steven.suib@uconn.edu; fax, (+1) (860) 486-2981.

Notes

The authors declare no competing financial interest.

ACKNOWLEDGMENTS

S.L.S. acknowledges the support of the U.S. Department of Energy, Office of Basic Energy Sciences, Division of Chemical, Biological and Geological Sciences, under grant DE-FG02-86ER13622.A000. J.H. acknowledges the financial support of startup funds from the University of Connecticut. This work was partially supported by the Green Emulsions Micelles and Surfactants (GEMS) Center.

REFERENCES

(1) Yano, J.; Kern, J.; Sauer, K.; Latimer, M. J.; Pushkar, Y.; Biesiadka, J.; Loll, B.; Saenger, W.; Messinger, J.; Zouni, A. *Science* **2006**, *314*, 821−825.

(2) Najafpour, M. M.; Ehrenberg, T.; Wiechen, M.; Kurz, P. *Angew. Chem., Int. Ed.* **2010**, *49*, 2233−2237.

(3) Robinson, D. M.; Go, Y. B.; Greenblatt, M.; Dismukes, G. C. *J. Am. Chem. Soc.* **2010**, *132*, 11467−11469.

(4) Jiao, F.; Frei, H. *Energy Environ. Sci.* **2010**, *3*, 1018−1027.

(5) Iyer, A.; Del-Pilar, J.; King'ondu, C. K.; Kissel, E.; Garces, H. F.; Huang, H.; El-Sawy, A. M.; Dutta, P. K.; Suib, S. L. *J. Phys. Chem. C* **2012**, *116*, 6474−6483.

(6) Boppana, V. B. R.; Jiao, F. *Chem. Commun.* **2011**, *47*, 8973−8975.

(7) Najafpour, M. M. *Dalton Trans.* **2011**, *40*, 3805−3807.

(8) Meng, Y.; Song, W.; Huang, H.; Ren, Z.; Chen, S.-Y.; Suib, S. L. *J. Am. Chem. Soc.* **2014**, *136*, 11452−11464.

(9) Jin, K.; Park, J.; Lee, J.; Yang, K. D.; Pradhan, G. K.; Sim, U.; Jeong, D.; Jang, H. L.; Park, S.; Kim, D.; Sung, N.-E.; Kim, S. H.; Han, S.; Nam, K. T. *J. Am. Chem. Soc.* **2014**, *136*, 7435−7443.

(10) Indra, A.; Menezes, P. W.; Zaharieva, I.; Baktash, E.; Pfrommer, J.; Schwarze, M.; Dau, H.; Driess, M. *Angew. Chem., Int. Ed.* **2013**, *52*, 13206−13210.

(11) Kuo, C. H.; Li, W.; Pahalagedara, L.; El-Sawy, A. M.; Kriz, D.; Genz, N.; Guild, C.; Ressler, T.; Suib, S. L.; He, J. *Angew. Chem., Int. Ed.* **2015**, *54*, 2345−2350.

(12) Robinson, D. M.; Go, Y. B.; Mui, M.; Gardner, G.; Zhang, Z.; Mastrogiovanni, D.; Garfunkel, E.; Li, J.; Greenblatt, M.; Dismukes, G. C. *J. Am. Chem. Soc.* **2013**, *135*, 3494−3501.

(13) Zaharieva, I.; Chernev, P.; Risch, M.; Klingan, K.; Kohlhoff, M.; Fischer, A.; Dau, H. *Energy Environ. Sci.* **2012**, *5*, 7081−7089.

(14) Yamaguchi, A.; Inuzuka, R.; Takashima, T.; Hayashi, T.; Hashimoto, K.; Nakamura, R. *Nat. Commun.* **2014**, *5*, 4256.

(15) Takashima, T.; Hashimoto, K.; Nakamura, R. *J. Am. Chem. Soc.* **2012**, *134*, 1519−1527.

(16) Park, J.; Kim, H.; Jin, K.; Lee, B. J.; Park, Y.-S.; Kim, H.; Park, I.; Yang, K. D.; Jeong, H.-Y.; Kim, J.; Hong, K. T.; Jang, H. W.; Kang, K.; Nam, K. T. *J. Am. Chem. Soc.* **2014**, *136*, 4201−4211.

(17) Najafpour, M. M.; Moghaddam, A. N.; Dau, H.; Zaharieva, I. *J. Am. Chem. Soc.* **2014**, *136*, 7245−7248.

(18) Jiao, F.; Frei, H. *Angew. Chem., Int. Ed.* **2009**, *48*, 1841−1844.

(19) Jiao, F.; Frei, H. *Chem. Commun.* **2010**, *46*, 2920−2922.

(20) Rosen, J.; Hutchings, G. S.; Jiao, F. *J. Am. Chem. Soc.* **2013**, *135*, 4516−4521.

(21) Poyraz, A. S.; Kuo, C.-H.; Biswas, S.; King'ondu, C. K.; Suib, S. L. *Nat. Commun.* **2013**, *4*, 2952.

(22) Gao, M.; Sheng, W.; Zhuang, Z.; Fang, Q.; Gu, S.; Jiang, J.; Yan, Y. *J. Am. Chem. Soc.* **2014**, *136*, 7077−7084.

(23) Poyraz, A. S.; Song, W.; Kriz, D.; Kuo, C.-H.; Seraji, M. S.; Suib, S. L. *ACS Appl. Mater. Interfaces* **2014**, *6*, 10986−10991.

(24) Han, Y.-F.; Chen, F.; Zhong, Z.; Ramesh, K.; Chen, L.; Widjaja, E. *J. Phys. Chem. B* **2006**, *110*, 24450−24456.

(25) Baddour-Hadjean, R.; Pereira-Ramos, J.-P. *Chem. Rev.* **2009**, *110*, 1278−1319.

(26) Wang, W.; Guo, S.; Lee, I.; Ahmed, K.; Zhong, J.; Favors, Z.; Zaera, F.; Ozkan, M.; Ozkan, C. S. *Sci. Rep.* 2014, *4*.

(27) Doyle, R. L.; Lyons, M. E. *Phys. Chem. Chem. Phys.* **2013**, *15*, 5224−5237.

(28) Ye, Z.-G.; Meng, H.-M.; Sun, D.-B. *J. Electroanal. Chem.* **2008**, *621*, 49−54.

(29) He, Z.; Mansfeld, F. *Energy Environ. Sci.* **2009**, *2*, 215−219.

(30) Tang, W.; Wu, X.; Li, D.; Wang, Z.; Liu, G.; Liu, H.; Chen, Y. *J. Mater. Chem. A* **2014**, *2*, 2544−2554.

(31) Liu, F.; Shan, W.; Lian, Z.; Xie, L.; Yang, W.; He, H. *Catal. Sci. Technol.* **2013**, *3*, 2699−2707.

(32) Gorlin, Y.; Lassalle-Kaiser, B.; Benck, J. D.; Gul, S.; Webb, S. M.; Yachandra, V. K.; Yano, J.; Jaramillo, T. F. *J. Am. Chem. Soc.* **2013**, *135*, 8525−8534.

(33) Karger, J.; Valiullin, R. *Chem. Soc. Rev.* **2013**, *42*, 4172−4197.

(34) Maeda, K. *ACS Catal.* **2014**, *4*, 1632−1636.

(35) Joo, J. B.; Zhang, Q.; Dahl, M.; Lee, I.; Goebl, J.; Zaera, F.; Yin, Y. *Energy Environ. Sci.* **2012**, *5*, 6321−6327.

DOI: 10.1021/cs501739e
ACS Catal. 2015, 5, 1693−1699